

HOSC: A Periodic Activation with Saturation Control for High-Fidelity Implicit Neural Representations

Michał Jan Włodarczyk

Warsaw University of Technology

michal.włodarczyk@pw.edu.pl

Danzel Serrano

New Jersey Institute of Technology

ds867@njit.edu

Przemysław Musalski

New Jersey Institute of Technology

przem@njit.edu

Abstract

Periodic activations such as sine preserve high-frequency information in implicit neural representations (INRs) through their oscillatory structure, but often suffer from gradient instability and limited control over multi-scale behavior. We introduce the Hyperbolic Oscillator with Saturation Control (HOSC) activation, $HOSC(x) = \tanh(\beta \sin(\omega_0 x))$, which exposes an explicit parameter β that controls the Lipschitz bound of the activation by $\beta \omega_0$. This provides a direct mechanism to tune gradient magnitudes while retaining a periodic carrier. We provide a mathematical analysis and conduct a comprehensive empirical study across images, audio, video, NeRFs, and SDFs using standardized training protocols. Comparative analysis against SIREN, FINER, and related methods shows where HOSC provides substantial benefits and where it achieves competitive parity. Results establish HOSC as a practical periodic activation for INR applications, with domain-specific guidance on hyperparameter selection. For code visit the project page: <https://hosc-nn.github.io/>.

1. Introduction

Implicit Neural Representations (INRs) have emerged as a powerful paradigm for signal encoding, replacing discrete grids with continuous coordinate-based functions learned by neural networks [23, 30, 32]. They represent a signal $s : \mathbb{R}^k \rightarrow \mathbb{R}^m$ with a coordinate-based neural network f_θ and are trained to minimize a reconstruction loss (plus regularization) over dense coordinate samples. Their promise—finite resolution, memory efficiency, and natural handling of irregular geometries—has driven rapid adoption across audio [31], video [6], image compression [8], and 3D reconstruction [20].

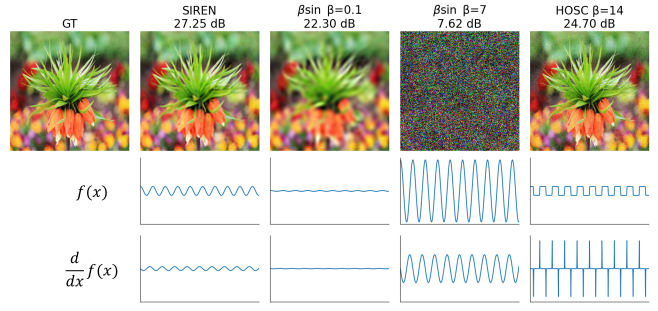


Figure 1. 2D image fitting with an identical coordinate MLP and fixed frequency $\omega_0 = 30$, varying the activation. From left to right: ground truth, SIREN $\sin(\omega_0 x)$, scaled sine $\beta \sin(\omega_0 x)$, and HOSC $\tanh(\beta \sin(\omega_0 x))$. SIREN and low- β sine underfit high-frequency detail, large- β sine produces unstable artifacts, while HOSC recovers sharp structure by combining high-frequency support with saturated, Lipschitz-controlled gradients.

Despite this success, INRs face a fundamental limitation: learning high-frequency components is inherently difficult for standard multilayer perceptrons, a phenomenon known as spectral bias [4, 14, 24]. Two main strategies have emerged to mitigate this: positional encoding methods [20, 32] that transform input coordinates to enhance high-frequency learning, and periodic activation functions [30] that directly improve representational capacity for oscillatory structure.

Within periodic activation designs, however, a fundamental architectural limitation persists. Fixed-period sine activations $\sin(\omega_0 x)$, as in SIREN [30], have activation-level Lipschitz constant $L_{\text{SIREN}} = \omega_0$, so the same parameter ω_0 simultaneously controls spectral support and gradient scale. Variable-periodic approaches such as FINER [17] address frequency flexibility through bias initialization and amplitude-dependent period, but do not provide a simple

global Lipschitz parameter: gradient behaviour remains inherited from the carrier frequency and internal modulation. As highlighted by recent benchmarking [14], the absence of an explicit, interpretable gradient-scale knob in periodic activations limits multi-modal adaptivity.

To address it, we introduce a *Hyperbolic Oscillator with Saturation Control* (HOSC), a periodic activation function with saturation control that enables explicit gradient tuning through a compositional design, defined as:

$$\text{HOSC}_\beta(x) = \tanh(\beta \sin(\omega_0 x)),$$

where ω_0 sets the carrier frequency and $\beta > 0$ controls saturation strength. This composition preserves periodic structure while inducing a tight activation-level Lipschitz constant $L_{\text{HOSC}} = \beta\omega_0$. In practice, ω_0 can be chosen for the desired spectral support as in SIREN, and β then acts as a single, interpretable parameter that multiplicatively scales gradients. HOSC thus provides a simple activation-level mechanism for per-modality gradient adaptation, without changing encodings or architecture, and with bounded outputs for numerical stability.

Figure 1 illustrates these behaviours on a 2D image: for a fixed network and carrier frequency, SIREN and low- β scaled sine yield oversmoothed reconstructions, a high- β scaled sine becomes unstable, whereas HOSC attains a sharp reconstruction by combining the same spectral support with controlled, saturated gradients. In summary, our contributions are:

- We propose HOSC, a periodic activation with saturation control that introduces an explicit activation-level Lipschitz parameter $L_{\text{HOSC}} = \beta\omega_0$, separating frequency selection (ω_0) from gradient scaling (β). In controlled ablations, we show that HOSC remains stable and improves reconstruction quality in β -regimes where scaled sine activations $\beta \sin(\omega_0 x)$ collapse.
- We provide a drop-in replacement for SIREN that requires no changes to positional encodings, remains compatible with standard SIREN-style initialization, and maintains bounded outputs for stable optimization.
- We validate HOSC across multiple modalities demonstrating significant performance gain on audio reconstruction and measurable improvements for video and images over prior periodic activations (SIREN, FINER), while providing competitive results on NeRFs and SDFs.

2. Related Work

2.1. INRs, Spectral Bias, and Periodic Activations

Implicit neural representations (INRs) parameterize continuous signals via coordinate MLPs and have been applied to images, videos, audio, and 3D geometry [20, 30, 32]. A central challenge is *spectral bias*: standard MLPs fit low frequencies first [4, 5, 24], which NTK theory explains

through eigenvalue decay of the kernel [10]. Fourier features [32] mitigate this by mapping coordinates through random Fourier embeddings that reshape the NTK into a stationary kernel with tunable bandwidth, thereby modifying the *frequency support* of the model.

SIREN [30] addresses spectral bias from the activation side by using fixed-period sine activations $\sin(\omega_0 z)$, with activation-level Lipschitz constant $L_{\text{act}} = \omega_0$ and bounded outputs. This improves representation of derivatives and PDE solutions, but the Lipschitz constant is entirely determined by ω_0 , so frequency support and gradient scale are coupled. Increasing ω_0 simultaneously increases the highest representable frequency and the upper bound on activation derivatives, leaving no separate control over gradient magnitudes during training.

2.2. Variable-Periodic, Gaussian, and Learned

Several works extend SIREN along the *frequency axis*. WIRE [27] introduces complex Gabor activations with superior joint space–frequency localization at the price of complex arithmetic and higher parameter counts. FINER [17] and FINER++ [33] propose variable-periodic activations of the form $\sin(\omega_0(|y| + 1)y)$ and show, via geometric and NTK analysis, that widening bias initialization ranges $b \sim \mathcal{U}(-k, k)$ lets the network select sub-functions with different effective frequencies. Conceptually, FINER tunes the *supported frequency set* through a combination of variable period and bias range k , but does not introduce an explicit global gradient or Lipschitz parameter: derivatives grow with $|z|$ and are not bounded by a single scalar. FINER++ extends this variable-periodic idea to Gaussian and wavelet carriers.

Orthogonal branches replace periodicity altogether. Gaussian activations [25] were shown to outperform sine on several INR tasks, and GARF [7] adapts Gaussian activations to NeRF. These works emphasize localization and gradient preservation rather than periodic structure. Sinc and related activations have also been studied from sampling-theoretic and functional-analytic perspectives [19, 28], but numerical issues near $x = 0$ limit practical adoption. More recently, meta-learned activation dictionaries (MIRE) [11] and functional architectures such as KAN [18] treat activation choice as a learning problem, confirming that activation geometry (including its Lipschitz and smoothness properties) strongly influences INR performance, but at the cost of additional infrastructure and complexity.

INR-Bench [14] systematically evaluates 56 coordinate-MLP variants and 22 KAN models across nine INR tasks, providing L-Lipschitz and L-smooth constants for common activations (e.g., $L_{\text{Lip}} = \omega$ for sine, $(1/\sigma)e^{-1/2}$ for Gaussians). Its main conclusion is that periodic sine combines favorable high-frequency learning in low-dimensional domains with a *fixed* activation Lipschitz constant, which lim-

its multi-scale adaptivity across modalities. This motivates activations with explicit, interpretable control over Lipschitz and gradient scale.

2.3. Architectural and Encoding Approaches

A different line of work targets multi-scale representation via *architecture* or *encoding*, rather than activation shape. Multiplicative Filter Networks and Residual MFN [9, 29] use multiplicative filters and skip connections to represent multiple scales, and ACORN and MINER [15, 26] decompose signals spatially or through mixture-of-experts to fit gigapixel images. InstantNGP [23] and Mip-NeRF variants [2, 3] show that multi-resolution hash grids and anti-aliasing encodings can dramatically accelerate NeRF and mitigate high-frequency artifacts. BACON [16] and anti-aliased SDF methods [34] achieve band-limited or LOD-controlled representations via encoding-level constraints, while NGSSF [21] uses Lipschitz-constrained MLPs together with modulated encodings to realize Gaussian scale spaces. Explicit-primitive approaches such as Neural Point Catacaustics [12] bypass INRs for certain phenomena (e.g., caustics) and thereby sidestep some low-frequency biases.

These methods primarily act along the *architectural/encoding* axis: they change how inputs are mapped and combined, not the local activation Lipschitz of a simple coordinate MLP. HOSC is designed to be orthogonal and compatible with such approaches: it modifies the activation while leaving encodings and architectures unchanged.

3. Method — HOSC

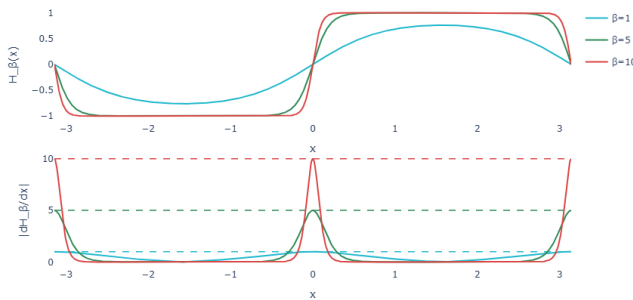


Figure 2. HOSC gradient control. Wrapping the sine in a hyperbolic tangent results in a periodic activation function that achieves saturation control through β . Derivative magnitude with Lipschitz bounds $L = \beta\omega_0$ (dashed). Increasing β amplifies and localizes gradients at zero-crossings while maintaining bounded outputs.

3.1. Hyperbolic Oscillator with Saturation Control

Our goal is to introduce a mechanism to decouple the gradient magnitude for different signal modalities or training regimes of a single periodic activation without sacrificing

the periodic structure. Wrapping the sine carrier in a hyperbolic tangent results in an oscillating activation function that achieves saturation control through a hyperbolic tangent:

$$\text{HOSC}_\beta(x) = \tanh(\beta \sin(\omega_0 x))$$

where $\beta > 0$ controls saturation strength and ω_0 determines carrier frequency. This composition introduces two key properties: (1) bounded outputs $|\text{HOSC}_\beta(x)| \leq 1$, and (2) tunable gradient magnitude through the β parameter.

Figure 2 visualizes HOSC for varying β values. At low $\beta < 1$, the tanh saturation is weak, producing near-linear behavior around zero and compressed oscillations at extrema. At high $\beta > 5$, saturation becomes aggressive, approximating a square wave with sharp transitions. This behavior enables HOSC to interpolate between smooth periodic functions (low β) and step-like responses (high β), providing flexibility across signal types requiring different frequency-detail tradeoffs.

3.2. Gradient Analysis and Lipschitz Bounds

To understand HOSC’s gradient flow properties, we compute its first derivative using the chain rule. For $\text{HOSC}_\beta(x) = \tanh(\beta \sin(\omega_0 x))$, we obtain:

$$\frac{d}{dx} \text{HOSC}_\beta(x) = \beta \omega_0 \cos(\omega_0 x) \cdot \text{sech}^2(\beta \sin(\omega_0 x))$$

where $\text{sech}^2(z) = 1/\cosh^2(z) = 1 - \tanh^2(z)$. This derivative exhibits three key characteristics: (1) multiplicative scaling by $\beta\omega_0$, (2) periodic oscillation via $\cos(\omega_0 x)$, and (3) amplitude modulation through $\text{sech}^2(\cdot)$ that depends on the sine carrier’s current value.

Activation-level Lipschitz constant. Since $|\cos(\omega_0 x)| \leq 1$ for all x and $0 < \text{sech}^2(z) \leq 1$ for all $z \in \mathbb{R}$ (with equality at $z = 0$), we obtain a tight Lipschitz bound:

$$\left| \frac{d}{dx} \text{HOSC}_\beta(x) \right| \leq \beta\omega_0$$

This bound is achieved precisely when $\sin(\omega_0 x) = 0$ (making $\text{sech}^2(0) = 1$) and $\cos(\omega_0 x) = \pm 1$, which occurs at $x = k\pi/\omega_0$ for integer k . The activation-level Lipschitz constant $L = \beta\omega_0$ bounds the derivative magnitude at each nonlinearity during backpropagation.

3.3. Layer and Network Gradient Bounds

Having established the scalar activation-level Lipschitz bound $L_{\text{HOSC}} = \beta\omega_0$ for the activation function, we now examine how this property propagates through multi-layer networks—a critical step for understanding HOSC’s impact on training dynamics.

From activation to layer. For a standard MLP layer computing $y = \text{HOSC}_\beta(\mathbf{W}\mathbf{x} + \mathbf{b})$, the chain rule decomposes the gradient into activation and linear components. Since

the activation-level Jacobian satisfies $\|\nabla_{\mathbf{z}} \text{HOSC}_{\beta}(\mathbf{z})\|_2 \leq \beta|\omega_0|$, the full layer gradient is bounded by

$$\|\nabla_{\mathbf{x}} \mathbf{y}\|_2 \leq \beta|\omega_0| \|\mathbf{W}\|_2$$

where $\|\mathbf{W}\|_2$ is the spectral norm of the weight matrix. This shows that gradient scale at each layer is jointly controlled by the activation parameter β and weight magnitude—enabling practitioners to adjust β to compensate for large weights without retraining.

Deep network composition. Stacking L such layers, the network-level Lipschitz constant satisfies the multiplicative upper bound

$$L_{\text{net}} \leq \prod_{\ell=1}^L \beta|\omega_0| \|\mathbf{W}_{\ell}\|_2.$$

This bound reveals why β acts as a global gradient scaling knob: reducing β by half reduces this upper bound on the network Lipschitz constant by a factor of 2^{-L} , providing exponential control over gradient magnitudes in deep architectures.

3.4. Asymptotic Behavior and Practical Regimes

To understand HOSC’s behavior across the full β -spectrum—from smooth near-linear responses to sharp square-wave transitions—we analyze limiting cases and relate them to the regimes that empirically arise in our experiments.

Smooth regime ($\beta \rightarrow 0$). For small β , a Taylor expansion of the outer tanh yields $\text{HOSC}_{\beta}(x) \approx \beta \sin(\omega_0 x)$, recovering a gently scaled sine with small derivative magnitude. In this regime, gradients remain smooth and relatively uniform, which empirically aligns with the behaviour we observe on high-dimensional coordinate tasks such as video and NeRF, where smaller β values lead to stable optimization (Sec. 4).

Sharp regime ($\beta \rightarrow \infty$). Conversely, as β grows large, the activation approaches the square-wave limit $\text{HOSC}_{\beta}(x) \rightarrow \text{sign}(\sin(\omega_0 x))$, and the derivative concentrates in narrow neighborhoods around the zeros of $\sin(\omega_0 x)$. This produces highly localized, high-magnitude gradients that are well suited to fitting sharp transitions. In our one-dimensional audio experiments, moderate-to-large β values exploit this effect and substantially improve reconstruction of rapid waveform variations (Sec. 4).

Gating width. The derivative $\text{HOSC}'_{\beta}(x) = \beta\omega_0 \cos(\omega_0 x) \text{sech}^2(\beta \sin(\omega_0 x))$ contains a $\text{sech}^2(\beta \sin(\cdot))$ factor that compresses gradients away from the zeros of the sine carrier. For thresholds proportional to the peak derivative, e.g. $\tau = \kappa\beta\omega_0$ with fixed $\kappa \in (0, 1)$, one can show (cf. Appendix A.4) that the measure of the superlevel set $\{x : |\text{HOSC}'_{\beta}(x)| \geq \tau\}$ scales on the order of $1/\beta$. Thus increasing β narrows the region where gradients

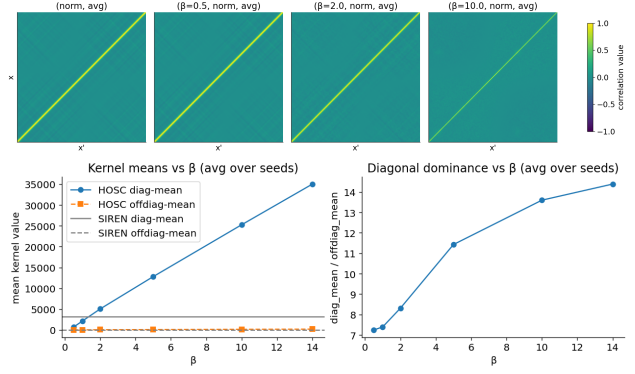


Figure 3. Empirical NTK behaviour of HOSC. *Top:* Correlation-normalized kernels for SIREN and HOSC with $\beta \in \{0.5, 2, 10\}$, averaged over multiple seeds. Larger β sharpens the diagonal and attenuates off-diagonal structure. *Bottom:* Mean diagonal values and diagonal-dominance ratio (diag / off-diagonal std) as a function of β . Both increase steadily, indicating that β acts as a controllable kernel-scale and interaction-strength knob.

are large while simultaneously raising their maximum magnitude, providing a controllable trade-off between gradient strength and spatial coverage that we exploit differently across modalities in Sec. 4.

Mathematical properties. For completeness, we note that HOSC inherits the sine carrier’s $2\pi/\omega_0$ -periodicity and odd symmetry, while adding bounded outputs $\text{HOSC}_{\beta}(x) \in [-1, 1]$ and C^{∞} -smoothness. The activation-level Lipschitz bound $L_{\text{act}} = \beta\omega_0$ is tight: at $x = k\pi/\omega_0$, for integer k , we have $\sin(\omega_0 x) = 0$, $\text{sech}^2(0) = 1$, and $|\text{HOSC}'_{\beta}(x)| = \beta\omega_0$.

3.5. NTK view of HOSC- β

To complement the Lipschitz analysis, we inspect the empirical NTK in a simple one-hidden-layer INR with shared random parameters. On a 1D grid $\{x_i\}$ we compute $K_{\theta}(x_i, x_j)$ for SIREN and for HOSC at different β , averaging over several seeds.

Because β rescales K_{θ} , we normalize by the diagonal and examine the correlation kernel $\tilde{K}_{ij} = K_{ij}/\sqrt{K_{ii}K_{jj}}$. Figure 3 (top) shows that for small β the HOSC NTK is nearly indistinguishable from SIREN, while larger β slightly sharpens the diagonal band and attenuates off-diagonal correlations.

We summarize this behaviour with two scalar statistics (Fig. 3, bottom): the mean diagonal of K_{θ} increases almost linearly with β , and a diagonal-dominance measure (diagonal mean divided by off-diagonal standard deviation) grows monotonically. In this one-layer setting, β therefore acts as a controllable kernel-scale and interaction-strength knob, smoothly shifting the kernel from a SIREN-like regime at small β toward a more self-dominated regime at larger β .

3.6. Relationship to SIREN

A natural question is whether HOSC provides capabilities beyond standard sinusoidal activations, or in other words: *why HOSC cannot be reduced to a rescaled or reparameterized SIREN?* The fundamental difference lies in parameter coupling: SIREN’s single parameter ω_0 simultaneously determines both the spectral support (which frequencies the network can represent) and the gradient magnitude during backpropagation.

This coupling means that increasing ω_0 to capture higher frequencies necessarily amplifies gradients, limiting adaptability. HOSC breaks this coupling through its compositional design $\tanh(\beta \sin(\omega_0 x))$, where ω_0 sets the carrier frequency while β provides an independent multiplicative gradient control. This decoupling enables stable training in high-gradient regimes ($\beta > 5$) that cause instability in amplitude-scaled sine networks. We verify this distinction through two controlled ablations.

Ablation 1: amplitude scaling (β -sin control). We test whether the \tanh envelope is essential by comparing HOSC against a direct amplitude-scaled sine $\beta \sin(\omega_0 x)$ under identical training conditions (Fig. 4). While both behave similarly at small β , the unscaled sine rapidly destabilizes as β increases, whereas HOSC remains stable. This confirms that the saturating envelope—not mere amplitude scaling—enables trainability in high-gradient regimes.

Ablation 2: frequency tuning (β -vs- ω_0). We test whether SIREN can match HOSC through aggressive frequency tuning by varying β for HOSC and ω_0 for SIREN over matched ranges (Fig. 5). While both show performance peaks, HOSC consistently achieves higher reconstruction quality, demonstrating that β ’s gradient control cannot be emulated through frequency reparameterization alone.

These ablations confirm: (1) HOSC is not a β -scaled sine, and (2) HOSC is not equivalent to frequency-tuned SIREN. The \tanh -sine composition provides a distinct gradient-control mechanism that neither amplitude scaling nor frequency reparameterization can replicate.

3.7. Relationship to FINER

FINER [17] addresses spectral bias from a different axis than HOSC. Rather than modifying the Lipschitz behaviour of a fixed-frequency sine, FINER introduces a *variable-periodic* activation of the form

$$\sigma_{\text{FINER}}(x) = \sin(\omega_0 \alpha(x) x), \quad \alpha(x) = |x| + 1, \quad (1)$$

and tunes the supported frequency set by widening the bias initialization $b \sim \mathcal{U}(-k, k)$. Geometric and NTK analyses in [17] show that increasing k selects sub-functions with higher effective frequencies, enlarges the supported frequency set $F_{\omega_0, k}$, and enhances NTK diagonal dominance, thereby improving high-frequency convergence.

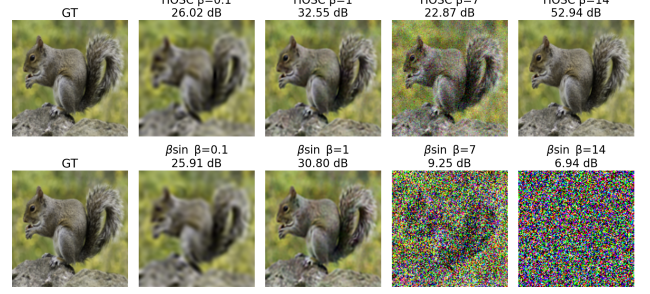


Figure 4. Effect of β for HOSC and β -sin. Single DIV2K image, $\omega_0 = 30$. Top row: GT and HOSC for $\beta \in \{0.1, 1, 7, 14\}$. Bottom row: GT and β -sin for the same β . All runs use the same INR architecture and training setup.

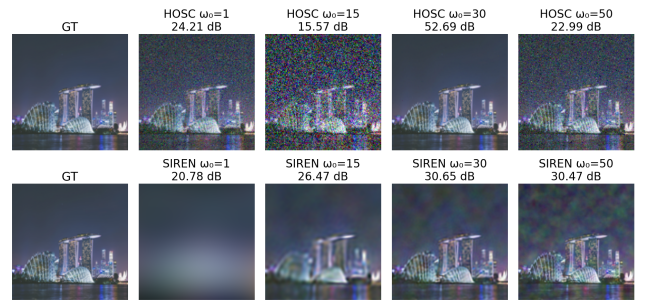


Figure 5. Effect of ω_0 for HOSC and SIREN. Single DIV2K image. Top row: HOSC with fixed $\beta = 14$ and $\omega_0 \in \{1, 15, 30, 50\}$. Bottom row: SIREN with $\beta = 1$ and the same ω_0 values, using the same INR architecture and training setup.

In contrast, HOSC keeps the carrier frequency fixed and instead wraps the sine with a saturating nonlinearity

$$\sigma_{\text{HOSC}}(x) = \tanh(\beta \sin(\omega_0 x)), \quad (2)$$

yielding a tight activation-level Lipschitz constant $\|\sigma'_{\text{HOSC}}\|_\infty = \beta \omega_0$ (Sec. 3). Thus HOSC introduces an explicit, global gradient-scale parameter β while leaving spectral support determined by ω_0 and the linear layers. FINER can be viewed as an *initialization-level frequency tuner*: it enlarges and redistributes the frequency set via bias range k and variable period $\alpha(x)$. HOSC is an *activation-level gradient tuner*: it provides bounded outputs and a controllable Lipschitz constant without altering the underlying frequency set. The two mechanisms are therefore orthogonal and, in principle, composable.

4. Practical Experiments

We examine HOSC’s reconstruction quality on tasks such as image, audio, video, NeRF and SDF reconstruction. In each experiment we first explore β parameter space with an ablation study. The best performing value is then used during method comparison. We compare HOSC with four activation-based INR methods, *i.e.* Gaussian (Gauss) [25],



Figure 6. Qualitative comparison on image fitting. Each row reconstructs the GT data with column specified method. Quantitative PSNR results showcased per example below reconstructed images. HOSC parameter $\beta = 14.0$.

Wavelet (WIRE) [27], Sine (SIREN) [30] and FINER [17] activations along with encoding based methods, *i.e.*, Fourier Features positional encoding (PEMLP) [32]. We report most notable results in the paper and present the details in the Appx. All experiments use a unified protocol with SIREN-style initialization, Adam, identical metrics, fixed seeds, deterministic dataloading, and consistent training schedules on A100/H100 GPUs.

4.1. Image Fitting

On 2D image reconstruction we aim to learn a mapping of 2D input pixel locations to 3D RGB output colors $f: \mathbb{R}^2 \rightarrow \mathbb{R}^3$, the loss function is the mean L_2 distance between the network output and the ground truth (MSE). We evaluate the reconstruction performance of the INR on 16 images from the DIV2k dataset [1] of 512×512 resolution. Firstly we ablate the β on all samples. We utilize the, on average, best performing β during the comparison with SoTA methods.

Findings. As shown in Tab. 1, the PSNR steadily increases with β and peaks around $\beta = 14.0$, after which it saturates or slightly degrades, so we fix $\beta = 14.0$ for all subsequent 2D image experiments. With this setting, HOSC clearly improves over PEMLP, Gauss, WIRE, and SIREN, and is competitive with FINER (Tab. 2): HOSC matches or exceeds FINER on 9 of the 16 images (see Appendix) while trailing it slightly on average. These results confirm that reaching a high- β regime is crucial to unlock HOSC’s advantages, and that in this regime HOSC closes most of the gap to the strongest existing periodic activation while

Table 1. **Image HOSC β -ablation.** Averaged over 16 samples. In experiment tables we color code each cell as **best**, **second best**, and **third best**.

HOSC β									
Metric PSNR \uparrow	0.1	0.2	0.5	0.8	1.0	2.0	4.0	5.0	
Mean	28.6934	31.8259	36.0805	37.2026	37.4394	38.7040	38.8871	38.6065	
Std	3.3241	2.9944	2.8315	2.9084	2.9572	3.4891	3.2364	3.0213	
	6.0	8.0	10.0	12.0	14.0	16.0	18.0	20.0	
Mean	38.5514	39.2204	39.9796	40.1840	40.2247	39.9558	39.1992	38.9566	
Std	2.9264	2.9735	2.8425	2.5163	2.3639	2.6917	2.6648	2.9618	

delivering substantial gains over standard sine-based INRs.

4.2. Audio Fitting

We evaluate the effectiveness of HOSC on the task of fitting an MLP to audio signals. The MLP learns an implicit 1D function, $f: \mathbb{R}^1 \rightarrow \mathbb{R}^1$ of signal amplitude with respect to time. The loss function is MSE. We evaluate the reconstruction quality on two examples, the first 7 seconds of Bach’s Cello Suite No. 1: Prelude (Bach) and a 12 second clip of a male actor counting 0-9 (Counting). We present Bach results in the paper and Counting in the Appendix.

Findings. The β -ablation in Tab. 3 shows that β in the range 4–5 yields the best reconstruction quality across both signals; we fix $\beta = 5.0$ as a single setting for all audio experiments. With this choice, HOSC substantially improves over all baselines (Tab. 4): compared to the next best activation (SIREN), HOSC reduces MSE by more than $4 \times$ on Bach and nearly an order of magnitude on Counting. This makes the audio setting the clearest example where entering the high- β regime unlocks a level of fidelity that sinusoidal activations alone cannot reach.

Table 2. **Quantitative comparison on image fitting.** Mean. and Std. values averaged over sixteen test set examples. $\beta = 14.0$.

Example PSNR \uparrow	PEMLP	Gauss	WIRE	SIREN	FINER	HOSC
Temple	26.3002	31.4108	28.0027	33.6837	35.8982	36.6901
Market	30.4807	35.8760	32.4138	40.2123	42.6105	40.3085
Wallnut	24.1596	32.2588	26.9073	34.4519	36.9627	37.0417
Mean	29.5525	35.6942	31.3934	38.5811	40.8816	40.2247
Std	3.7192	2.7251	3.0141	3.1956	3.1379	2.3639

Table 3. **Audio HOSC β -ablation.** Showcased for Bach and Counting examples. Full ablation in the Appendix

HOSC β						
Example MSE \downarrow	1.0	2.0	4.0	5.0	6.0	8.0
Bach	9.86e-06	2.029e-06	7.589e-07	1.319e-06	2.384e-06	2.138e-05
Counting	4.328e-04	2.550e-04	6.851e-05	3.613e-05	9.355e-05	1.707e-04



Figure 7. Qualitative comparison on video fitting. A 300 frame video of a cat was reconstructed. Displayed is a single frame from the video. Quantitative results showcased per example below reconstructed frames. HOSC $\beta = 0.5$.

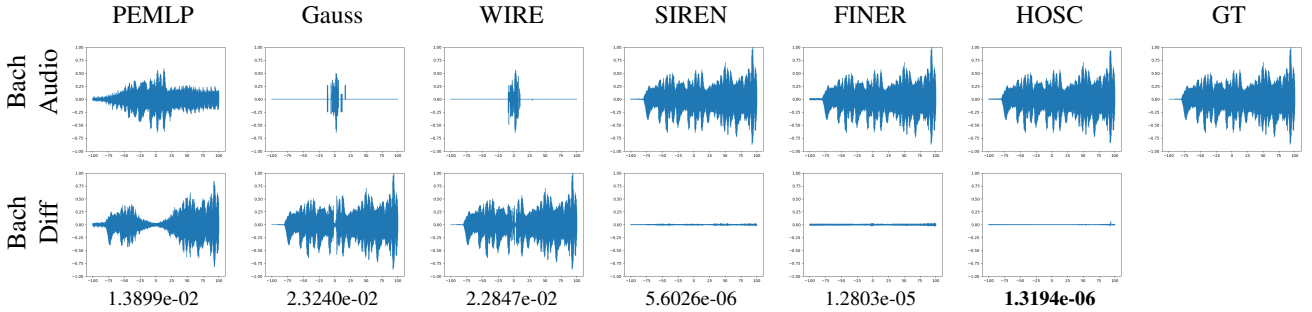


Figure 8. Qualitative comparison on audio fitting. We visualize the reconstructed signal (Audio) and the difference of predicted and GT signal (Diff). We quantify the difference with MSE. HOSC $\beta = 5.0$.

4.3. Video Fitting

We evaluate HOSC’s effectiveness on video reconstruction, where an MLP parameterizes a function $f : \mathbb{R}^3 \rightarrow \mathbb{R}^3$ mapping (x, y, t) to RGB values. The loss is mean squared error (MSE). We use a 300-frame cat video at 512×512 resolution and report per-frame and average PSNR/MSE. All methods share the same network architecture, optimizer, training schedule, and initialization; only the activation (and β for HOSC) differs. We first ablate β and then compare HOSC to PEMLP, Gauss, WIRE, SIREN, and FINER using the best β .

Findings. The β -ablation in Tab. 5 shows a clear optimum at $\beta = 0.5$; smaller or larger values reduce reconstruction quality. With this choice, HOSC achieves the best overall performance (Tab. 6): it improves PSNR by about 3 dB and halves the MSE relative to SIREN, while non-periodic baselines lag further behind. This aligns with our analysis that (cf. Sec. 3.4), for higher-dimensional coordinate inputs such as (x, y, t) , a relatively small β keeps HOSC in a smoothly saturated, sine-like regime that yields stable and

accurate reconstructions.

4.4. Neural Radiance Fields (NeRF)

We evaluate HOSC and other activations based methods on the Blender benchmark (8 scenes) [20]. All methods share the same architecture, optimizer, training budget, and SIREN-style initialization; no positional encodings are used. We ablate the HOSC β parameter and compare under identical budgets on PSNR, SSIM and LPIPS metrics.

Findings. The β -ablation in Tab. 7 shows that NeRF performance peaks for $\beta \in [0.5, 1.0]$; larger values quickly degrade PSNR/SSIM and LPIPS, with $\beta \geq 3$ leading to severe collapse across all scenes (Tab. 7). With β chosen in this low range, HOSC matches SIREN and FINER on the Blender benchmark (Tab. 8), with per-scene PSNR differences on the order of 0.1–0.2 dB (FINER 29.84 dB, HOSC 29.74 dB, SIREN 29.71 dB). In NeRF, the main benefit of HOSC is thus a safe, explicit gradient-scale knob that pre-

Table 5. **Video HOSC β -ablation.** Showcased for the Cat video.

Metric	HOSC β				
	0.1	0.5	1.0	2.0	5.0
MSE \downarrow	7.7876e-04	5.5673e-04	6.7687e-04	1.5408e-02	1.6507e-01
PSNR \uparrow	37.3071	38.71367	37.821784	24.2534	13.9256

Table 6. Quantitative comparisons on video fitting. $\beta = 0.5$

Metric	PEMLP	Gauss	WIRE	SIREN	FINER	HOSC
MSE \downarrow	2.3615e-03	1.8921e-03	3.8377e-03	1.0487e-03	2.4904e-03	5.5673e-04
PSNR \uparrow	32.3877	33.3167	30.2326	35.9106	32.1581	38.7137



Figure 9. Qualitative comparison on image fitting. SSIM metric showcased under each method for the Lego truck example from the NeRF Synthetic dataset[20]. HOSC $\beta = 1.0$.

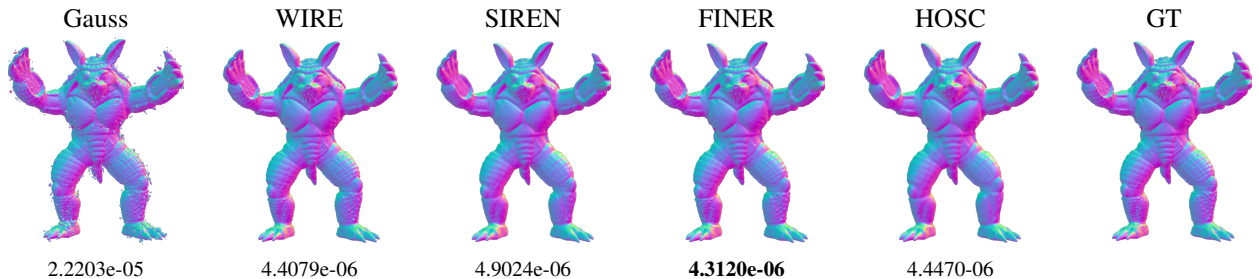


Figure 10. Qualitative comparison on signed distance field (Neural SDF) fitting. Chamfer Distance showcased per example below the reconstructed shape. $\beta = 0.8$. We provide full results, along with an ablation study and experimental details in the Appendix.

serves the frequency support of sine-based INRs, rather than a new accuracy regime as in our audio experiments.

4.5. Signed Distance Fields

We next test HOSC on 3D signed distance field (SDF) reconstruction, where an MLP parameterizes a function $f: \mathbb{R}^3 \rightarrow \mathbb{R}$ whose zero-level set defines a surface. Following prior work [16, 34], we train all methods to minimize a point-to-surface loss and report Chamfer distance on held-out surface samples. We show a representative qualitative comparison on the `Armadillo` shape in Fig. 10, together with per-method Chamfer distances. Additional shapes and a small β -sweep for HOSC are reported in the Appendix.

Findings. On `Armadillo`, HOSC achieves a chamfer distance that is on par with periodic baselines and clearly improves over non-periodic activations (Fig. 10): Gaussian is an order of magnitude worse, while WIRE, SIREN, FINER, and HOSC all lie in a narrow band around.

Table 7. **NeRF HOSC β -ablation.** Averaged over eight sample from NeRF Synthetic [20]

HOSC β							
Stat.	0.1	0.3	0.5	0.8	1.0	3.0	5.0
PSNR	26.4848	28.7892	29.3195	29.6461	29.7321	26.7590	21.6911
	4.5546	4.4083	4.4643	4.6295	4.6157	4.0048	3.1601
SSIM	0.9002	0.9300	0.9346	0.9372	0.9388	0.9033	0.7999
	0.0765	0.0652	0.0629	0.0640	0.0622	0.0579	0.0820
LPIPS	0.1157	0.0455	0.0393	0.0358	0.0353	0.0757	0.2355
	0.0835	0.0374	0.0318	0.0282	0.0277	0.0427	0.0768

5. Conclusions

We introduced HOSC, a periodic activation that decouples gradient scale from the carrier frequency and adds an explicit gradient-gating mechanism. Analytically, we derived tight activation-level Lipschitz bounds, showed that the high-gradient region shrinks as $O(1/\beta)$, and related β to the structure of the empirical NTK, which becomes increasingly diagonal-dominant as gradients localize. These results turn β into a simple but effective knob for controlling both stability and locality in implicit neural representations.

Empirically, HOSC acts as a drop-in replacement for sine activations. The gains are strongest on 1D audio, where high carrier frequencies are beneficial over SIREN

Table 8. **Quantitative comparisons on novel view synthesis.** HOSC $\beta = 1.0$

Methods	Chair	Drums	Ficus	Hotdog	Lego	Materials	Mic	Ship
PSNR \uparrow	PEMLP	29.33	20.11	23.33	28.32	24.56	23.80	22.59
	Gauss	29.33	22.51	25.45	29.59	25.98	24.87	31.51
	WIRE	33.86	25.08	27.85	34.18	29.41	27.85	34.95
	SIREN	34.39	25.75	28.45	33.96	30.26	27.81	35.08
	FINER	34.77	25.91	28.86	33.58	30.76	27.74	35.05
	HOSC	34.28	25.83	28.36	33.77	30.49	27.86	35.28
SSIM \uparrow	PEMLP	0.950	0.823	0.907	0.925	0.893	0.907	0.931
	Gauss	0.940	0.851	0.932	0.919	0.892	0.902	0.970
	WIRE	0.976	0.915	0.958	0.971	0.949	0.945	0.982
	SIREN	0.978	0.923	0.960	0.969	0.958	0.946	0.982
	FINER	0.977	0.923	0.962	0.967	0.959	0.943	0.982
	HOSC	0.977	0.925	0.961	0.968	0.960	0.946	0.983
LPIPS \downarrow	PEMLP	0.039	0.180	0.078	0.054	0.085	0.069	0.121
	Gauss	0.042	0.109	0.057	0.082	0.061	0.086	0.024
	WIRE	0.015	0.053	0.033	0.018	0.034	0.032	0.015
	SIREN	0.014	0.046	0.029	0.023	0.024	0.030	0.0132
	FINER	0.012	0.043	0.027	0.028	0.021	0.031	0.011
	HOSC	0.014	0.045	0.030	0.027	0.023	0.031	0.014

and FINER. On images and videos HOSC behaves like a mild regularizer yielding smaller but robust improvements. On NeRF it matches frequency-tuned baselines while remaining stable at more aggressive hyper-parameters. Overall, our results suggest that explicitly designing activations for controllable Lipschitz constants and localized gradients is complementary to frequency-based INR architectures. As future work, we aim to develop activations and architectures that achieve an even fuller decoupling between frequency content and gradient control, for example via learnable carriers or spatially adaptive gating in high-dimensional neural fields.

References

- [1] Eirikur Agustsson and Radu Timofte. Ntire 2017 challenge on single image super-resolution: Dataset and study. In *The IEEE Conference on Computer Vision and Pattern Recognition (CVPR) Workshops*, 2017. [6](#), [12](#)
- [2] Jonathan T. Barron, Ben Mildenhall, Matthew Tancik, Peter Hedman, Ricardo Martin-Brualla, and Pratul P. Srinivasan. Mip-NeRF: A multiscale representation for anti-aliasing neural radiance fields. In *Proceedings of the IEEE/CVF International Conference on Computer Vision (ICCV)*, pages 5855–5864, 2021. [3](#)
- [3] Jonathan T. Barron, Ben Mildenhall, Dor Verbin, Pratul P. Srinivasan, and Peter Hedman. Mip-nerf 360: Unbounded anti-aliased neural radiance fields. In *IEEE/CVF Conference on Computer Vision and Pattern Recognition (CVPR)*, pages 5460–5469, 2022. [3](#)
- [4] Ronen Basri, Meirav Galun, Amnon Geifman, David Jacobs, Yoni Kasten, and Shira Kritchman. Frequency bias in neural networks for input of non-uniform density. In *Proceedings of the International Conference on Machine Learning (ICML)*, pages 685–694. PMLR, 2020. [1](#), [2](#)
- [5] Yuan Cao, Zhiying Fang, Yue Wu, Ding-Xuan Zhou, and Quanquan Gu. Towards understanding the spectral bias of deep learning. *arXiv preprint arXiv:1912.01198*, 2019. [2](#)
- [6] Hao Chen, Bo He, Hanyu Wang, Yixuan Ren, Ser-Nam Lim, and Abhinav Shrivastava. Nerv: Neural representations for videos. In *Advances in Neural Information Processing Systems 34: Annual Conference on Neural Information Processing Systems 2021, NeurIPS 2021*, pages 21557–21568, 2021. [1](#)
- [7] Shin-Fang Chng, Sameera Ramasinghe, Jamie Sherrah, and Simon Lucey. Gaussian activated neural radiance fields for high fidelity reconstruction and pose estimation. In *European Conference on Computer Vision (ECCV)*, pages 264–280, 2022. [2](#)
- [8] Emilien Dupont, Adam Goliński, Milad Alizadeh, Yee Whye Teh, and Arnaud Doucet. COIN: COmpression with implicit neural representations. In *Neural Compression Workshop at ICLR 2021*, 2021. *arXiv:2103.03123*. [1](#)
- [9] Rizal Fathony, Anit Kumar Sahu, Devin Willmott, and J. Zico Kolter. Multiplicative filter networks. In *International Conference on Learning Representations (ICLR)*, 2021. [3](#)
- [10] Arthur Jacot, Franck Gabriel, and Clément Hongler. Neural tangent kernel: Convergence and generalization in neural networks. In *Advances in Neural Information Processing Systems (NeurIPS)*, pages 8580–8589. Curran Associates, Inc., 2018. [2](#)
- [11] Dhananjaya Jayasundara, Heng Zhao, Demetrio Labate, and Vishal M. Patel. Mire: Matched implicit neural representations. In *IEEE/CVF Conference on Computer Vision and Pattern Recognition (CVPR)*, pages 8279–8288, 2025. [2](#)
- [12] Georgios Kopanas, Thomas Leimkühler, Gilles Rainer, Clément Jambon, and George Drettakis. Neural point catacaustics for novel-view synthesis of reflections. *ACM Transactions on Graphics*, 41(6), 2022. SIGGRAPH Asia 2022. [3](#)
- [13] Stanford Computer Graphics Laboratory. The stanford 3d scanning repository, 2014. <http://graphics.stanford.edu/data/3Dscanrep/>. [14](#)
- [14] Linfei Li, Fengyi Zhang, Zhong Wang, Lin Zhang, and Ying Shen. Inr-bench: A unified benchmark for implicit neural representations in multi-domain regression and reconstruction. *arXiv preprint arXiv:2510.10188*, 2025. [1](#), [2](#)
- [15] David B. Lindell, Dave Van Veen, Jeong Joon Park, and Gordon Wetzstein. ACORN: Adaptive coordinate networks for neural scene representation. *ACM Transactions on Graphics (TOG)*, 40(4), 2021. [3](#)
- [16] David B. Lindell, Dave Van Veen, Jeong Joon Park, and Gordon Wetzstein. Bacon: Band-limited coordinate networks for multiscale scene representation. In *IEEE/CVF Conference on Computer Vision and Pattern Recognition (CVPR)*, pages 16241–16250, 2022. [3](#), [8](#), [14](#)
- [17] Zhen Liu, Hao Zhu, Qi Zhang, Jingde Fu, Weibing Deng, Zhan Ma, Yanwen Guo, and Xun Cao. FINER: Flexible spectral-bias tuning in implicit neural representation by variable-periodic activation functions. In *Proceedings of the IEEE/CVF Conference on Computer Vision and Pattern Recognition (CVPR)*, pages 2713–2722, 2024. [1](#), [2](#), [5](#), [6](#), [12](#)
- [18] Ziming Liu, Yixuan Wang, Sachin Vaidya, Fabian Ruehle, James Halverson, Marin Soljačić, Thomas Y. Hou, and Max Tegmark. Kan: Kolmogorov-arnold networks. In *International Conference on Learning Representations (ICLR)*, 2025. Oral presentation. [2](#)
- [19] Lassi Meronen, Martin Trapp, and Arno Solin. Periodic activation functions induce stationarity. *Advances in Neural Information Processing Systems (NeurIPS)*, 34:2021–2032, 2021. [2](#)
- [20] Ben Mildenhall, Pratul P. Srinivasan, Matthew Tancik, Jonathan T. Barron, Ravi Ramamoorthi, and Ren Ng. NeRF: Representing scenes as neural radiance fields for view synthesis. In *Proceedings of the European Conference on Computer Vision (ECCV)*, pages 405–421. Springer, 2020. [1](#), [2](#), [7](#), [8](#), [14](#)
- [21] Felix Muykanovic, Ntumba Elie Nsampi, Christian Theobalt, Hans-Peter Seidel, and Thomas Leimkühler. Neural gaussian scale-space fields. *ACM Transactions on Graphics*, 43(4), 2024. SIGGRAPH 2024. [3](#)
- [22] Thomas Müller. tiny-cuda-nn, 2021. [14](#)

[23] Thomas Müller, Alex Evans, Christoph Schied, and Alexander Keller. Instant neural graphics primitives with a multiresolution hash encoding. *ACM Transactions on Graphics (TOG)*, 41(4):102:1–102:15, 2022. [1](#), [3](#), [14](#)

[24] Nasim Rahaman, Aristide Baratin, Devansh Arpit, Felix Draxler, Min Lin, Fred A. Hamprecht, Yoshua Bengio, and Aaron C. Courville. On the spectral bias of neural networks. In *Proceedings of the 36th International Conference on Machine Learning*, pages 5301–5310. PMLR, 2019. [1](#), [2](#)

[25] Sameera Ramasinghe and Simon Lucey. Beyond periodicity: Towards a unifying framework for activations in coordinate-mlps. In *European Conference on Computer Vision (ECCV)*, pages 142–158, 2022. Oral presentation. [2](#), [5](#), [12](#)

[26] Vishwanath Saragadam, Daniel LeJeune, Jasper Tan, Guha Balakrishnan, Ashok Veeraraghavan, and Richard G. Baraniuk. MINER: Multiscale implicit neural representation. In *Proceedings of the European Conference on Computer Vision (ECCV)*, pages 318–333. Springer, 2022. [3](#)

[27] Vishwanath Saragadam, Daniel LeJeune, Jasper Tan, Guha Balakrishnan, Ashok Veeraraghavan, and Richard G. Baraniuk. WIRE: Wavelet implicit neural representations. In *Proceedings of the IEEE/CVF Conference on Computer Vision and Pattern Recognition (CVPR)*, pages 18507–18516, 2023. [2](#), [6](#), [12](#)

[28] Hemanth Saratchandran, Sameera Ramasinghe, Violetta Shevchenko, Alexander Long, and Simon Lucey. A sampling theory perspective on activations for implicit neural representations, 2024. [2](#)

[29] Shayan Shekarforoush, David B. Lindell, David J. Fleet, and Marcus A. Brubaker. Residual multiplicative filter networks for multiscale reconstruction. In *Advances in Neural Information Processing Systems (NeurIPS)*, pages 23848–23860, 2022. [3](#)

[30] Vincent Sitzmann, Julien N. P. Martel, Alexander W. Bergman, David B. Lindell, and Gordon Wetzstein. Implicit neural representations with periodic activation functions. In *Advances in Neural Information Processing Systems (NeurIPS)*, pages 7462–7473. Curran Associates, Inc., 2020. [1](#), [2](#), [6](#), [12](#)

[31] Kun Su, Mingfei Chen, and Eli Shlizerman. Inras: Implicit neural representation for audio scenes. In *Advances in Neural Information Processing Systems*, pages 8144–8158. Curran Associates, Inc., 2022. [1](#)

[32] Matthew Tancik, Pratul P. Srinivasan, Ben Mildenhall, Sara Fridovich-Keil, Nithin Raghavan, Utkarsh Singhal, Ravi Ramamoorthi, Jonathan T. Barron, and Ren Ng. Fourier features let networks learn high frequency functions in low dimensional domains. In *Advances in Neural Information Processing Systems (NeurIPS)*, pages 7537–7547. Curran Associates, Inc., 2020. [1](#), [2](#), [6](#), [12](#)

[33] Hao Zhu, Zhen Liu, Qi Zhang, Jingde Fu, Weibing Deng, Zhan Ma, Yanwen Guo, and Xun Cao. FINER++: Building a family of variable-periodic functions for activating implicit neural representation. *arXiv preprint arXiv:2407.19434*, 2024. [2](#)

[34] Yiyu Zhuang, Qi Zhang, Ying Feng, Hao Zhu, Yao Yao, Xiaoyu Li, Yan-Pei Cao, Ying Shan, and Xun Cao. Anti-aliased neural implicit surfaces with encoding level of detail. In *SIGGRAPH Asia 2023 Conference Papers*, pages 1–10. ACM, 2023. [3](#), [8](#)

HOSC: A Periodic Activation with Saturation Control for High-Fidelity Implicit Neural Representations

Supplementary Material

Appendix Overview

This appendix first collects the mathematical details for HOSC activations, including formal statements and proofs for the results in Sec. 3. The subsequent sections provide practical information for the experiments: training and implementation details, ablations of the parameter β , and extended quantitative tables and qualitative visualizations for all image, audio, video, NeRF, and SDF experiments, as well as an additional hash-grid experiment. Qualitative results are available in an HTML experiment suite via the entry page (<https://hosc-nn.github.io/>).

A. Mathematical Details for HOSC

This part provides formal statements and proofs supporting the mathematical claims in Sec. 3.

Notation, assumptions, and terminology

Let $\beta > 0$ and $\omega_0 > 0$. Define the scalar activation

$$\phi_{\beta, \omega_0}(x) = \tanh(\beta \sin(\omega_0 x)).$$

For layers use $z = Wx + b$ and apply ϕ elementwise. Matrix norms are spectral ($\|\cdot\|_2$); Jacobian/operator norms are the induced ℓ_2 -norms. ‘‘Activation-level Lipschitz’’ is w.r.t. preactivation z . **Terminology note:** ‘‘Decouple’’ in the main text means introducing an independent knob β for gradient scale while ω_0 sets the carrier frequency; the activation-level Lipschitz equals $\beta\omega_0$ and depends on both.

A.1. Activation calculus and Lipschitz bound

Lemma A.1.1 (Derivative). For $f(x) = \phi_{\beta, \omega_0}(x)$,

$$f'(x) = \beta \omega_0 \cos(\omega_0 x) \operatorname{sech}^2(\beta \sin(\omega_0 x)).$$

Proof. Chain rule with $u(x) = \beta \sin(\omega_0 x)$ and $\frac{d}{dx} \tanh u = \operatorname{sech}^2 u \cdot u'$. \square

Lemma A.1.2 (Tight activation-level Lipschitz).

$$\sup_{x \in \mathbb{R}} |f'(x)| = \beta \omega_0.$$

Proof. From Lemma A.1.1, $|f'| \leq \beta \omega_0$ since $|\cos| \leq 1$ and $0 < \operatorname{sech}^2 \leq 1$. Equality at $x = k\pi/\omega_0$ where $\sin = 0$ and $|\cos| = 1$. \square

Corollary A.1.3 (Basic properties). ϕ_{β, ω_0} is $2\pi/\omega_0$ -periodic, odd, bounded in $[-1, 1]$, and C^∞ .

A.2. Layer and network bounds

Proposition A.2.1 (Layer Jacobian bound). For $y = \phi_{\beta, \omega_0}(Wx + b)$,

$$\|\nabla_x y\|_2 \leq \beta \omega_0 \|W\|_2 \quad \text{for all } x.$$

Proof. The Jacobian factors as $J = D(z)W$ with $D(z) = \operatorname{diag}(f'(z_i))$. By Lemma A.1.2, $\|D(z)\|_2 \leq \beta \omega_0$. Submultiplicativity gives $\|J\|_2 \leq \beta \omega_0 \|W\|_2$. \square

Proposition A.2.2 (Network Lipschitz upper bound). For an L -layer MLP y_L with $y_k = \phi_{\beta, \omega_0}(W_k y_{k-1} + b_k)$,

$$\|\nabla_x y_L(x)\|_2 \leq \prod_{k=1}^L (\beta \omega_0 \|W_k\|_2), \quad \forall x.$$

Proof. Apply Proposition A.2.1 to each layer and submultiplicativity to the Jacobian product. \square

A.3. Asymptotics in β

Proposition A.3.1 (Small- β expansion). For $\beta \in (0, \beta_0]$,

$$\phi_{\beta, \omega_0}(x) = \beta \sin(\omega_0 x) - \frac{\beta^3}{3} \sin^3(\omega_0 x) + O(\beta^5)$$

uniformly in x .

Proof. Taylor series $\tanh s = s - s^3/3 + O(s^5)$ with $s = \beta \sin(\omega_0 x)$ and $|\sin| \leq 1$. \square

Proposition A.3.2 (Large- β limit). If $\sin(\omega_0 x) \neq 0$, then $\phi_{\beta, \omega_0}(x) \rightarrow \operatorname{sign}(\sin(\omega_0 x))$ as $\beta \rightarrow \infty$; convergence holds pointwise a.e. and in L^p_{loc} for any finite p .

Proof. $\tanh y \rightarrow \operatorname{sign}(y)$ as $|y| \rightarrow \infty$. Take $y = \beta \sin(\omega_0 x)$. Dominated convergence yields local L^p convergence on compact sets away from zeros; boundedness by 1 provides domination. \square

A.4. Gating region measure

This section addresses Section 3.4 in the paper. Let

$$\begin{aligned} g_\beta(x) &= \beta \omega_0 |\cos(\omega_0 x)| \operatorname{sech}^2(\beta |\sin(\omega_0 x)|), \\ u &= \omega_0 x \in [0, 2\pi]. \end{aligned}$$

Lemma A.4.1 (Per-period active set under proportional thresholds). Fix $\kappa \in (0, 1)$ and define the proportional threshold

$$\tau_\beta = \kappa \beta \omega_0.$$

Over one period $I = [0, 2\pi/\omega_0]$, consider the superlevel set

$$S_\beta = \{x \in I : g_\beta(x) \geq \tau_\beta\}.$$

Then

$$|S_\beta| \leq \frac{4}{\omega_0} \arcsin\left(\min\left\{1, \frac{\operatorname{arccosh}(1/\sqrt{\kappa})}{\beta}\right\}\right),$$

and in particular $|S_\beta| = O(1/\beta)$ as $\beta \rightarrow \infty$.

Proof. Write $u = \omega_0 x$. The inequality

$$g_\beta(x) = \beta \omega_0 |\cos u| \operatorname{sech}^2(\beta |\sin u|) \geq \kappa \beta \omega_0$$

implies that $\operatorname{sech}^2(\beta |\sin u|) \geq \kappa$, since $|\cos u| \leq 1$. Thus a necessary condition for membership in S_β is

$$\operatorname{sech}^2(\beta |\sin u|) \geq \kappa \iff \beta |\sin u| \leq c_\kappa = \operatorname{arccosh}(1/\sqrt{\kappa}).$$

Hence

$$S_\beta \subset \left\{x \in I : |\sin(\omega_0 x)| \leq c_\kappa/\beta\right\}.$$

Over $u \in [0, 2\pi]$, the set $\{u : |\sin u| \leq \varepsilon\}$ consists of three intervals (near 0, π , and 2π) with total length $4 \arcsin(\varepsilon)$. Mapping back via $x = u/\omega_0$ gives

$$|S_\beta| \leq \frac{4}{\omega_0} \arcsin\left(\min\{1, c_\kappa/\beta\}\right).$$

As $\beta \rightarrow \infty$, we have $c_\kappa/\beta \rightarrow 0$ and therefore

$$\arcsin\left(\min\{1, c_\kappa/\beta\}\right) = \arcsin(c_\kappa/\beta) \sim c_\kappa/\beta,$$

which implies $|S_\beta| = O(1/\beta)$. \square

A.5. Tightness points

Lemma A.5.1 (Where the maximum slope is attained). $|f'(x)| = \beta \omega_0$ iff $x = k\pi/\omega_0$, $k \in \mathbb{Z}$. **Proof.** Simultaneously require $|\cos(\omega_0 x)| = 1$ and $\sin(\omega_0 x) = 0$. \square

A.6. Multivariate extension

For elementwise activations, $z = Wx + b \in \mathbb{R}^m$ and $y = \phi_{\beta, \omega_0}(z)$ applied elementwise, the diagonal Jacobian satisfies $\|\nabla_z y\|_2 \leq \beta \omega_0$ (Lemma A.1.2), yielding Proposition A.2.1 by composition with W .

B. Practical Experiments Details

All experiments were conducted under the same experimental regime described in the paper. At first an ablation study on the HOSC β parameter is conducted. After that a comparison with known methods is computed. For each experiment we present the implementation and experimental details along with additional results that have been omitted in the paper and left out for the supplemental.

Qualitative Results. For convenient inspection of our results we provide an HTML experiment suite in the supplemental material. The entry page (<https://hoscnn.github.io/>) links to per-experiment pages for image, audio, video, NeRF, and SDF fitting. Each page shows the same methods and test cases as the corresponding tables/figures and offers interactive browsing (e.g., image and video sliders, audio play–pause controls) with the best methods highlighted as in the quantitative results.

Source Code. We will publicly release the full source code for all experiments presented in this paper, including training scripts, evaluation pipelines, and the HTML experiment suite, to facilitate reproducibility and further research.

Method Comparison Setup. We compare HOSC with methods like PEMLP (FF) [32], Gauss [25], WIRE [27], [30] and FINER [17]. For each baseline method, the hyperparameters were configured according to the specifications provided in their original publications or as implemented in their respective reference codebases. Specifically, for PEMLP (FF), the Fourier Feature mapping utilized a total of 10 frequencies. The Gauss’s scale parameter was set to 30. The WIRE configuration involved setting both the initial (ω_0) and hidden (ω_h) ω parameters to 20, while the scale factor was set to 10. A common setup was employed for SIREN, where the initial ω_0 was set to 30 and all subsequent layer-wise ω parameters were uniformly set to 1. Finally, the specific parameter configuration for FINER was adopted directly from the setup described in its official implementation.

B.1. Image Fitting

Data. We utilize a 16 example subset from the testing set of the DIV2K Dataset [1]. Each image is of 512×512 resolution. Both the value range and input pixel coordinates are scaled to $[-1, 1]$. No additional preprocessing is done. We later rescale both ranges for inference and results collection.

Network & Hyperparameters. We use an MLP with 3 hidden layers, of 256 width, for all experiments on fitting images. We train for 5000 epochs, at each iteration we fit on every pixel of the GT image, batch size is equal to the number of pixels in the image. We use the Adam optimizer with a learning rate specific to each method, consistent throughout each trained sample. We utilize activation specific recommended learning rates. For FINER, SIREN and HOSC

Table 9. **Audio HOSC β -ablation.** Showcased for Bach and Counting examples.

Example MSE ↓	HOSC β							
	0.1	0.2	0.5	0.8	1.0	2.0	4.0	5.0
Bach	6.6636e-04	2.2016e-04	1.7386e-05	1.0024e-05	9.8558e-06	2.0293e-06	7.5893e-07	1.3194e-06
Counting	9.8662e-04	5.2919e-04	4.1339e-04	4.0398e-04	4.3283e-04	2.5501e-04	6.8511e-05	3.6126e-05
	6.0	8.0	10.0	12.0	14.0	16.0	18.0	20.0
Bach	2.3844e-06	2.1383e-05	9.4639e-05	4.3760e-04	2.3118e-02	2.4166e-02	2.4180e-02	2.4184e-02
Counting	9.3554e-05	1.7069e-04	8.9352e-04	6.7790e-03	7.2318e-03	7.0961e-03	7.3637e-03	7.3835e-03

Table 10. **Seed Independence.** Seed independence evaluation of HOSC and related methods.

Example MSE ↓	SIREN		FINER		HOSC	
	Mean	Std	Mean	Std	Mean	Std
Bach	5.6905e-06	3.9998e-07	1.2704e-3	4.0961e-03	7.1032e-07	5.8887e-08
Counting	3.853e-04	4.5750e-06	2.8612e-03	1.6933e-03	4.4506e-05	5.6223e-06

we use a $LR = 5e - 04$, for Gauss and WIRE we use a $LR = 5e - 03$ and for PEMLP we use a $LR = 1e - 3$. We conducted experiments on consistent learning rates on all methods and found out that the mentioned rates achieve a better reconstruction quality.

Hardware & Runtime. The networks are trained using a single NVIDIA A100 GPU with 40GB of memory. We train for 5,000 epochs, requiring approximately 3 minutes to fit and evaluate a single image. For the ablation study we consider 256 configurations which all amount to 16hrs of training. The comparison study took 4.8hrs of training.

B.2. Audio Fitting

Data. For learning audio signals we use two samples; the first 7 seconds from Bach’s Cello Suite No. 1, representing music data and a stock audio of a male actor counting from 0 to 9, representing human speech data. Audio signals are taken from waveform files sampled at 44100 samples per second. Both value and coordinates are scaled to the range of $[-1, 1]$. We use all sample points as training data. We provide additional results for the Counting sample in the HTML experiments suite (<https://hosc-nn.github.io/>) and an extended β parameter ablation in Tables 3 and 9.

Network & Hyperparameters. We use an MLP with 3 hidden layers, of 256 width, for all experiments on fitting audio. We train for 5000 epochs, at each iteration we fit on the whole audio wave, batch size is equal to the number sample tick. We use the Adam optimizer with a learning rate specific to each method, exactly the same as in the setup for image experiments.

Hardware & Runtime. The networks are trained using a single NVIDIA A100 GPU with 40GB of memory. We train for 5,000 epochs, requiring approximately 2 minutes to fit and evaluate a single audio waveform. For the ablation study we consider 90 configurations which all amount to 30 minutes of training. The comparison study took 1hrs of training.

Seed Independence. We evaluate the impact of seed choice on the quality of result by training audio reconstruction models on a finite set of chosen seeds: $\{0, 2, 4, 8, 12, 21, 42, 1337, 3333, 3407, 2025\}$. We see a very small dependency on seed for both SIREN and HOSC, while FINER due to its inherent reliance on initialization is considerably influence by the seed change, see Tab. 10.

B.3. Video Fitting

Data. For learning videos we use a single video of a Cat which contains 300 frames of 512×512 resolution. The value range is scaled to $[-1, 1]$. Full Quantitative results are available in the paper.

Network & Hyperparameters. We use an MLP with 5 hidden layers, of 1024 width, for all experiments on fitting video. We train for 100 000 epochs, at each iteration we fit on the whole video at once, batch size is equal to the whole video size. We use the Adam optimizer with a learning rate of $1e - 04$ consistent across all methods. We found that method specific learning rates used for image and audio reconstruction, achieved inconclusive results. While on method specific learning rates PEMLP achieved a PSNR of 37.12 outperforming SIREN, the other methods struggled to achieve a PSNR of over 14.00. In the paper we present

Table 11. **Quantitative comparisons.** Averaged over eight NeRF Synthetic [20] samples.

	Stat.	PEMLP	Gauss	WIRE	SIREN	FINER	HOSC
PSNR	Mean.	23.9840	26.1985	29.2248	29.7097	29.8378	29.7321
	Std.	3.4295	3.7701	4.9856	4.6224	4.5956	4.6157
SSIM	Mean.	0.8811	0.8877	0.9303	0.9371	0.9371	0.9388
	Std.	0.0779	0.0852	0.0772	0.0653	0.0660	0.0622
LPIPS	Mean.	0.1078	0.0856	0.0485	0.0355	0.0352	0.0353
	Std.	0.0681	0.0617	0.0575	0.0302	0.0313	0.0277

results for consistent learning rate comparisons only.

Hardware & Runtime. The networks are trained using a single NVIDIA H100 GPU with 80GB of memory. We train for 100 000 epochs, requiring approximately 10hrs to fit and evaluate a single video. For the ablation study we consider 5 configurations which all amount to 50hrs of training. The comparison study took 60hrs of training.

B.4. Neural Radiance Fields (NeRF)

Data. In Neural Radiance Fields experiments we use the NeRF Synthetic Dataset [20] consisting of 8 examples. We utilized the experimental setting described in WIRE where only 25 images are used for training, and each image is downsampled to a resolution of 200×200 , 4x downampling from the original 800×800 .

Network & Hyperparameters. We use an MLP with 4 layers, of 182 width, for all NeRF experiments. We train for 37500 iterations. We use the Adam optimizer with a scheduled learning rate starting from $2e-4$ and finishing at $1e-15$, consistent across all methods. We don't consider method specific learning rates, due to the learning rate schedulers influence.

Hardware & Runtime. The networks are trained using a single NVIDIA A100 GPU with 40GB of memory. We train for 30 000 iterations, requiring approximately 30 minutes to fit and evaluate a single NeRF. For the ablation study we consider 56 configurations which all amount to approximately 30hrs of training. The comparison study took 15hrs of training.

B.5. Signed Distance Fields

Data. In Signed Distance Fields experiments we use samples from the Stanford 3D Scanning Repository [13], the Armadillo, Dragon, Thai Statue and Lucy. Model vertices are normalized to fit inside the unit cube.

Network & Hyperparameters. We use an MLP with 3 layers, of 256 width, for all SDF experiments. We use the Adam optimizer with a scheduled learning of $1e-04$, consistent across all methods. The coarse-to-fine loss function

[16] is used. Training takes 200 000 iterations. In each iteration 10 000 points are randomly sampled and fed to the model. For visualization 512^3 grid is extracted.

Hardware & Runtime. The networks are trained using a single NVIDIA A100 GPU with 40GB of memory. We train for 200 000 iterations, requiring approximately 3hrs to fit and evaluate a single SDF. For the ablation study we consider 11 configurations which all amount to approximately 30hrs of training. The comparison study took 24hrs of training.

B.6. Orthogonality to encoding methods

To validate HOSC's scalability and address the relationship between activation design and spatial encoding methods, we implemented HOSC in both PyTorch and *Tiny-Cuda-NN* [22] and trained on gigapixel-scale images. We compare HOSC against activation-based methods (SIREN, PEMLP) and Instant-NGP's HashGrid encoding [23], which represents the state-of-the-art for large-scale spatial data. Results are shown in Fig. 12 and Tables 14, 15.

Data. For gigapixel image fitting experiments we use the “Girl With a Pearl Earring” painting renovation ©Koorosh Ooroj (CC BY-SA 4.0) at 8000×9302 resolution.

Network & Hyperparameters. We use an MLP with 3 hidden layers of 256 width. We use the Adam optimizer with a learning rate of 1×10^{-4} , consistent across methods. We compare four methods: PEMLP, SIREN, HOSC, and the HashGrid encoding from Instant-NGP [23]. Training is done for 1000 epochs with a batch size of 2,000,000 ($\approx 3\%$ of the entire image).

Hardware & Runtime. The networks are trained using a single NVIDIA A100 GPU with 40GB of memory. Training for 1000 epochs requires approximately 3 hours per configuration. The β -ablation study (Table 14) involves 10 configurations totaling approximately 30 hours. The comparison study (Table 15) required 21 hours total.

Results: HOSC vs activation baselines. HOSC achieves **23.45 dB PSNR** in PyTorch and 22.71 dB in TCNN (Table 15), outperforming SIREN (23.19 dB / 21.67 dB) and PEMLP (23.03 dB / 22.51 dB) in both frameworks. The

Table 12. **Signed Distance Field HOSC β -ablation.** Experiment on the Armadillo shape.

Metric	HOSC β										
	0.1	0.3	0.5	0.8	0.9	1.0	3.0	5.0	8.0	12.0	16.0
Chamfer	5.280e-06	4.814e-06	5.638e-06	4.447e-06	5.581e-06	4.324e-06	5.676e-06	6.057e-06	5.877e-06	5.293e-06	7.673e-06
IoU	0.9774	0.9778	0.9728	0.9817	0.9762	0.9821	0.9738	0.9729	0.9734	0.9808	0.9670

Table 13. **Quantitative comparisons on SDF reconstruction.** HOSC $\beta = \{0.8, 0.9, 1.0\}$

	Samples	Gauss	WIRE	SIREN	FINER	HOSC $\beta = 0.8$	HOSC $\beta = 0.9$	HOSC $\beta = 1.0$
Chamfer \rightarrow	Armadillo	2.2065e-05	4.3975e-06	4.8958e-06	4.3178e-06	4.4470e-06	5.5813e-06	4.3237e-06
	Dragon	1.9011e-05	2.5875e-06	3.1763e-06	3.0937e-06	3.3799e-06	3.9059e-06	3.7843e-06
	Thai	3.7762e-05	2.8232e-05	3.1437e-05	2.9137e-05	3.0911e-05	3.2658e-05	3.1313e-05
	Lucy	2.5397e-05	2.1952e-05	2.2656e-05	2.2189e-05	2.2966e-05	2.3785e-05	2.2929e-05
IoU \uparrow	Armadillo	0.9766	0.9799	0.9775	0.9809	0.9817	0.9762	0.9821
	Dragon	0.9506	0.9617	0.9584	0.9610	0.9546	0.9508	0.9498
	Thai	0.8310	0.8328	0.8338	0.8297	0.8366	0.8326	0.8229
	Lucy	0.8625	0.8719	0.8731	0.8692	0.8727	0.8675	0.8724

β -ablation (Table 14) demonstrates robustness across $\beta \in [0.5, 12.0]$, with PyTorch achieving peak performance at $\beta = 5.0$ (23.45 dB) and TCNN at $\beta = 8.0$ (22.71 dB). Visual results (Fig. 12) show HOSC produces high-fidelity reconstructions competitive with SIREN and PEMLP across both implementations.

Results: HOSC vs spatial encoding (INGP). Instant-NGP’s HashGrid encoding achieves 25.19 dB (Table 15), approximately 2 dB higher than activation-based methods. This gap is expected: HashGrid employs a multi-resolution hash table that explicitly models spatial coherence, whereas HOSC (and all activation functions) operates on individual coordinates without spatial structure. Critically, HOSC and HashGrid are **orthogonal design choices**—HashGrid is an input encoding, HOSC is an activation function—and could potentially be combined in future work.

Discussion. Trade-offs and when to use HOSC. While HashGrid excels on large-scale spatial data (images, NeRF), it requires domain-specific architectural modifications and additional memory for the hash table. HOSC provides a simpler, activation-based alternative that works across diverse domains without specialized encodings: the same activation achieves strong results on images (Sec. 4.1), audio (Sec. 4.2), video (Sec. 4.3), NeRF (Sec. 4.4), and SDFs (Sec. 4.5). For applications where architectural simplicity, multi-domain generality, or explicit gradient control via β are priorities, HOSC offers a compelling alternative. The consistent performance across PyTorch and TCNN implementations (Table 15) further demonstrates HOSC’s robustness and practical applicability.

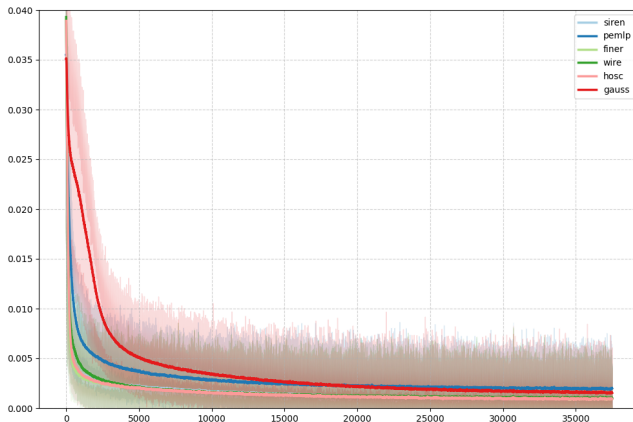


Figure 11. **Method specific loss curves.** Average over all examples computed for NeRF experiments.

Table 14. **Gigapixel HOSC β -ablation.**

Framework	HOSC β				
	0.5	1.0	5.0	8.0	12.0
TCNN	21.05	21.73	22.57	22.71	22.69
PyTorch	23.20	23.09	23.45	22.70	22.50

Table 15. **Quantitative comparison for Gigapixel reconstruction.**

Metric	TCNN			PyTorch			
	INGP	PEMLP	SIREN	HOSC	PEMLP	SIREN	HOSC
PSNR	25.19	22.51	21.67	22.71	23.03	23.19	23.45

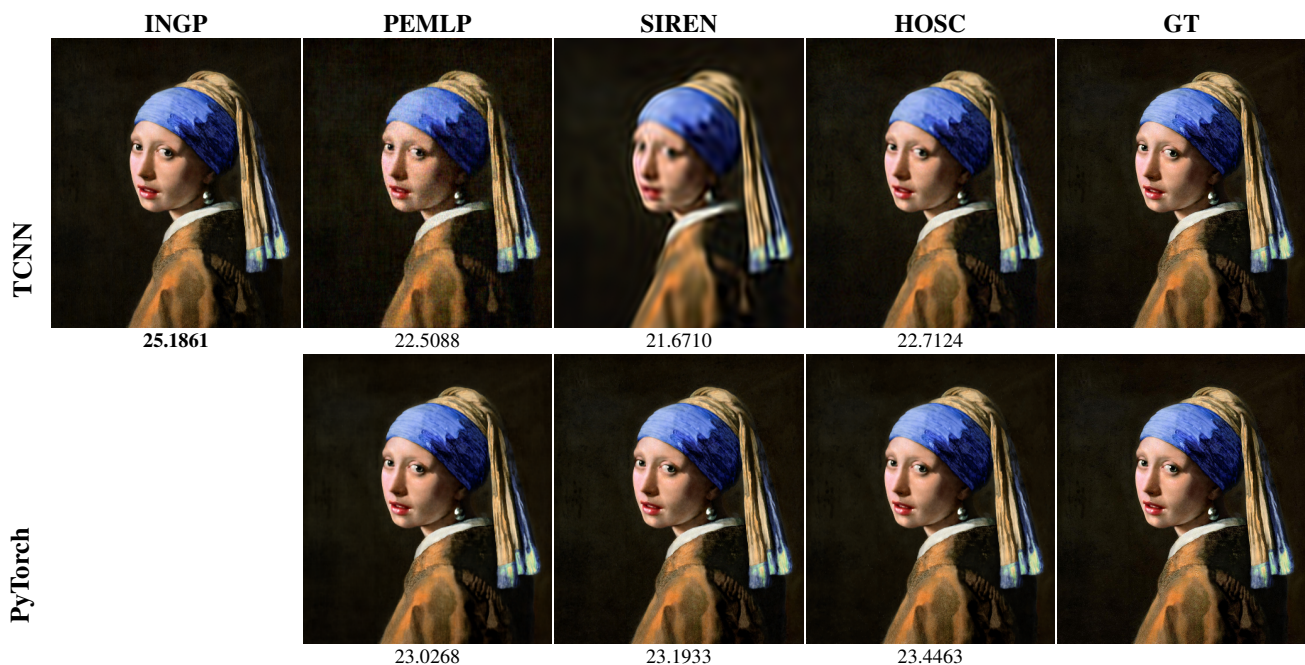


Figure 12. Qualitative comparison on Gigapixel reconstruction. Each row reconstructs the GT data with column specified method. Quantitative (PSNR) results showcased per example below reconstructed images. HOSC $\beta = 8.0$. for TCNN and $\beta = 5.0$ for PyTorch.